# Mannheimer and Schechter model revisited: Viscosimetry of a (non-)Newtonian and curved interface

Kévin Patouillet

*Univ. Grenoble-Alpes, CNRS, Grenoble-INP (Institute of Engineering Univ. Grenoble Alpes),*
*SIMAP, F-38000 Grenoble, France*
*and Linamar-Montupet, Light Metal Casting Division, Techcenter 3 rue de Nogent, 60290 Laigneville, France*

Laurent Davoust,[*] Olivier Doche, and Jules Delacroix

*Univ. Grenoble-Alpes, CNRS, Grenoble-INP (Institute of Engineering Univ. Grenoble Alpes),*
*SIMAP, F-38000 Grenoble, France*

The impact of a Newtonian or non-Newtonian interface, possibly curved due to wetting effects, on the surface viscosimetry method historically developed by Mannheimer and Schechter [Mannheimer and Schechter, J. Colloid Interface Sci. **32**, 195 (1970); **32**, 212 (1970)] is investigated theoretically and numerically in this paper. The Reynolds number is considered small enough for inertial effects to be negligible and thus for surface shear viscosity to be preferentially studied. The classical Boussinesq-Scriven law is modified by a shear-dependent viscosity governed by the Carreau constitutive law. The case of a curved interface is also investigated whether the liquid is hydrophilic or hydrophobic (liquid metals), which is revealed to be relevant for a liquid with a significant capillary length. The shallow-channel layout is found to be particularly well suited to the detection of a non-Newtonian liquid surface whatever its mechanical behavior: shear thinning or shear thickening. A key to evaluating the parameters involved in a surface viscosity model is to carry out a series of experiments at various rotation speeds, with preferably a nonwetting contact angle. Indeed, it is demonstrated that such a contact angle tends to amplify non-Newtonian effects, especially for a carrier fluid with a significant capillary length.

## I. INTRODUCTION

When a liquid-gas interface is composed of a heterogeneous chemical content, introduction of surface rheology is relevant for the description of its mechanical behavior. According to the Gibbs hypothesis, rheological properties of the interface can be described using a macroscopic approach (see [1]). To compensate for the appearance of a jump in stresses due to the zero thickness of the interface considered as a two-dimensional (2D) medium, (excess) surface quantities are introduced: the surface shear viscosity $\eta_\sigma$, the surface dilatational viscosity $\chi_\sigma$, and the surface tension $\gamma$.

Nowadays, research is increasingly focusing on assessing the impact of these rheological parameters on multiphase flows (e.g., foams, drops, bubbles, and thin films). This is accounted for by the frequent use of surfactants, proteins, or amphiphilic nanoparticles in the sectors of life sciences [2–4], cosmetics, microfluidics, food, and feed industry, particularly aimed at simplifying the formation and stabilization of emulsions and foams [5–8]. Recently, the introduction of surface rheology has been proved to be relevant for modeling a liquid or molten metal flow covered

---

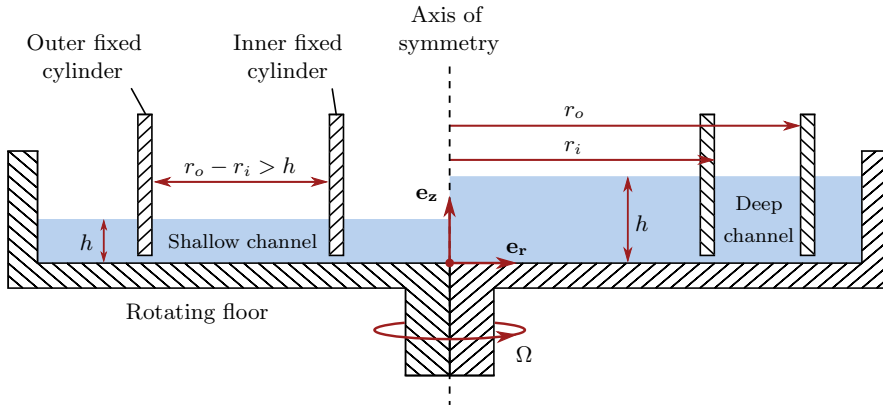[*]Corresponding author: laurent.davoust@simap.grenoble-inp.fr

054002-1

FIG. 1. Cross section of the annular surface viscometer considering the shallow-channel configuration on the left-hand side and the deep-channel layout on the right-hand side.

by an oxide film [9,10]. During the continuous casting process, liquid metals tend to oxidize instantaneously on contact with the ambient air. A thin oxide layer, approximately 100 nm to 1 $\mu$m thick, forms at the air-metal interface. With respect to either a layer of adsorbed molecules or an oxide film, it is commonly accepted that the rheological properties of the interface greatly depend on film structure and thickness. Generally speaking, a higher concentration of surfactants or a more advanced oxidation level leads to a reduction in surface tension, combined with an increase in surface viscosities.

Since the start of the 20th century, many authors have worked on the implementation of experimental test benches in order to measure these surface quantities at micro- or macroscale [11] and evaluate their impact. Harkins and Meyers [12] proposed the first surface viscometer able to measure surface shear viscosity due to a flow induced by an interfacial pressure gradient. However, this technique does not avoid the Marangoni effect. To guard against a potential surface tension gradient in the flow direction, Mannheimer and Schechter [13] developed the classical configuration of the annular viscometer. In this system, whose cross section is shown on the right-hand side of Fig. 1, an annular shear flow is end driven by a rotating floor between two motionless sidewalls. The inner and outer radii are $r_i$ and $r_o$, respectively, and the height of the liquid is denoted by $h$.

Many authors have since used and revisited this technique to determine preferentially surface shear viscosity [14–17]. In fact, for small to moderate Reynolds numbers, the meridional flow due to centrifugation is vanishingly small and the flow is azimuthal. Consequently, only surface shear viscosity is solicited. Recently, some authors have looked into the possibility of using this system to determine surface dilatational viscosity due to sufficiently high rotation speeds [18–20]. Inertial effects are no longer negligible and the meridional flow, resulting from centrifugation, means that surface dilatational viscosity is also solicited. However, surface flow may cause a radially inward packing of the adsorbed elements to the inner part of the viscometer. Should this occur, interfacial properties are no longer uniformly distributed along the interface and a Marangoni stress could be suspected. In particular, an analytical study has proved the influence of a radial distribution of molecules at the interface on the azimuthal surface flow [21].

In most cases, the Boussinesq-Scriven model [22], based on a Newtonian interface, is sufficient to correctly describe the mechanical behavior of an interface in a permanent regime. When implemented in a jump momentum balance (JMB), evaluated at the interface, it establishes the relation between surface stresses and volumic stresses [23]. However, just as for bulk properties of certain fluids, interface properties may depend on flow conditions (beyond the mere fact that the flow regime is permanent, oscillatory, or transient). Several authors have already experimentally observed a reduction in surface viscosity with the increase in shear rate at the interface via an
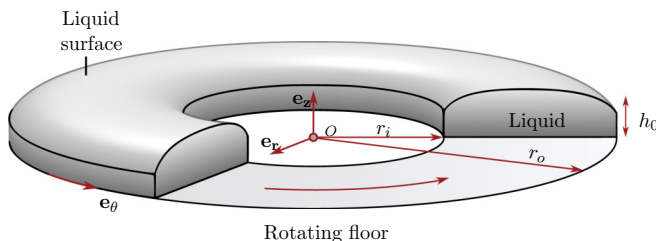
FIG. 2. Three-dimensional representation of the liquid flowing in the annular viscometer with an example of curved interface (inner radius $r_i = 3$ cm, outer radius $r_o = 7$ cm, and average liquid depth $h_0 = 1$ cm).

interfacial rheometer [24–26] or with the classical annular viscometer configuration [27,28]. A velocity gradient along the interface can cause molecular rearrangements, generally resulting in a reduction in surface flow resistance. According to this work, an interface populated by active agents may have a behavior of the shear-thinning type [29,30], in the same way as fluids such as blood [31,32], and certain polymer solutions [33,34] whose apparent dynamic viscosity decreases as shear rate increases.

Likewise, the hypothesis of a planar interface is often put forward as a means of markedly simplifying the tangential JMB expression. This hypothesis is completely justified when the capillary length of the carrier fluid is short compared with channel width or when the fluid wets the sidewalls and when a technique involving a sharp edge with precise monitoring of bath height is implemented [13]. Otherwise (see Fig. 2), Wasan and co-workers [14,35] have highlighted, analytically (with some approximations) and experimentally, the influence of interface curvature on the surface velocity field. Thus, identification of surface shear viscosity may be falsified, whether or not the mechanical behavior of the surface is Newtonian. While Hirsa and co-workers [15,18,28–30] investigated the role of a large Reynolds number in channel viscosimetry, the goal of the present paper is to demonstrate the role of curvature effects. This is particularly relevant in the case where the liquid under consideration exhibits a contact angle larger than 90° (liquid metals, for instance) and more generally speaking in the case where the contact angle is time dependent because of surface aging or evaporation.

## II. GOALS AND OVERALL METHOD

In this paper we propose a theoretical and numerical study of the coupling between the mechanics of a non-Newtonian and curved interface with a carrier annular flow. To promote bulk-surface coupling, preference is given to the shallow-channel layout (see the left part of Figs. 1 and 2), corresponding to the case where the liquid depth is reduced compared with the radial gap of the channel, over the classic annular viscometer configuration.

In point of fact, this geometric aspect ratio amplifies the coupling between the surface viscous effects and those of the subphase due to higher vertical bulk shear. Similarly, a reduction in channel height causes an increase in tangent shear along the free surface, thereby encouraging the emergence of non-Newtonian behavior. With respect to the surface viscosity model, the idea is simply to use one of the many models for describing non-Newtonian fluid behavior and to extend it to the case of an interface populated by active agents or covered by an oxide film.

Thus, the first aim is to investigate the two-way coupling between a non-Newtonian liquid-gas interface and an annular flow. The two mechanical behaviors for a liquid surface, shear thinning and shear thickening, are investigated and the detection range of a non-Newtonian behavior within the annular viscometer is discussed. The second aim consists in determining the influence of the surface curvature that is not always negligible, particularly for liquid metals. Its impact on the identification process of surface shear viscosity, uniformly distributed or otherwise, is evaluated by considering two different subphases: an aqueous solution and a molten aluminium bath.

In the following, the hypotheses, governing equations, and boundary conditions are first highlighted. Special attention is given to the jump momentum balance, written for the general case of a nonuniform and curved interface. Then the non-Newtonian surface viscosity model and the scaling parameters of the problem are defined. Numerical modeling, based on the finite-element method, is benchmarked with Mannheimer and Schechter's analytical solution, considering a Newtonian planar interface. Finally, the impact of a non-Newtonian curved interface is highlighted and discussed.

### III. PHYSICAL MODELING

#### A. Notation and hypotheses

Regarding purely hydrodynamic hypotheses, annular flow is assumed to be axisymmetric ($\partial \boldsymbol{\cdot} /\partial \theta = 0$), permanent, and laminar with an incompressible and Newtonian carrier fluid. The Reynolds number $\mathrm{Re} = \rho \Omega r_o^2 / \eta$, with $\rho$ the subphase density, $\eta$ its dynamic viscosity, and $\Omega$ the rotation speed of the rotating floor, is considered sufficiently small for inertial effects to be negligible, typically $\mathrm{Re} \leqslant 200$. Below this limit value assessed in [18], the radial and the vertical components of the velocity field are negligible, which means that the flow can be considered purely azimuthal: $\mathbf{v} = v_\theta(r, z)\mathbf{e}_\theta$. Creeping annular flow, considered to be in steady state, is thus governed by the azimuthal component of the Stokes equation

$$\frac{\partial}{\partial r}\left(\frac{1}{r}\frac{\partial(r v_\theta)}{\partial r}\right) + \frac{\partial^2 v_\theta}{\partial z^2} = 0. \tag{1}$$

Several hypotheses are then made concerning the liquid-gas interface mechanics. First, just as in the Mannheimer and Schechter model, the flow is supposed to be purely azimuthal and hence the deformation of the interface due to an eventual radial pressure gradient induced by centrifugation is consistently considered to be negligibly small.[1] As already mentioned, the role of inertia has been extensively investigated in the recent literature [15,18,20,28], whereas the present paper aims at investigating the ability of surface curvature to modify surface viscosity identification. Among other consequences, the surface dilatational viscosity $\chi_\sigma$ is not solicited, allowing preferential focus on the role of the surface shear viscosity $\eta_\sigma$. However, in contrast to the existing literature, the hypothesis of a planar interface is not considered here, which allows us to consider a contact angle at the sidewalls as well as a significant capillary length, typically of the same order as the length scale of the channel,

$$l_c = \sqrt{\frac{\gamma}{\rho g}} \sim r_o - r_i. \tag{2}$$

In this expression, $\gamma$ is the surface tension, $g$ is the gravity, and $r_o - r_i$ is the radial gap of the channel. As an example, one can consider a nonwetting liquid metal such as molten aluminium whose capillary length is found to be approximately 6 mm at 750 °C.

In the following, the shape of the liquid surface is determined by taking gravity, surface tension, and wetting angle into account. The index $\sigma$ is used to denote surface quantities and the symbol $\theta$ refers to the azimuthal direction.

---

[1]In [20], the elevation of the liquid surface is measured by a digital particle image velocimetry technique with a Reynolds number as large as $\mathrm{Re} = 8500$. Hirsa *et al.* demonstrate that even with such a level of inertia, the maximum change in surface elevation is no larger than $50 \pm 10$ $\mu$m. As a consequence, the shape of the interface is neither modified by an eventual radial pressure gradient nor subjected to a significant normal viscous stress (with a capillary number as small as $\mathrm{Ca} \sim 10^{-5}$).

## B. Interfacial hydrodynamics

### 1. Surface stress tensor

The macroscopic description of the interface requires introduction of the surface (in-excess) stress tensor supplied by the Boussinesq-Scriven constitutive law [1]

$$\overline{\overline{T}}_\sigma = [\gamma + (\chi_\sigma - \eta_\sigma)\mathrm{div}_\sigma(\mathbf{v}_\sigma)]\overline{\overline{P}} + \eta_\sigma\{\overline{\overline{P}} \cdot [\overline{\overline{\mathrm{grad}}}_\sigma(\mathbf{v}_\sigma)] + [\overline{\overline{\mathrm{grad}}}_\sigma(\mathbf{v}_\sigma)]^\top \cdot \overline{\overline{P}}\}. \tag{3}$$

Here $\overline{\overline{P}}$ stands for the surface projection tensor, defined as $\overline{\overline{P}} = \overline{\overline{I}} - \mathbf{n} \otimes \mathbf{n}$, where $\overline{\overline{I}}$ is the identity matrix and $\mathbf{n}$ is the normal unit vector at the interface defined as

$$\mathbf{n} = \frac{-h'}{\sqrt{1 + h'^2}}\mathbf{e_r} + \frac{1}{\sqrt{1 + h'^2}}\mathbf{e_z}, \tag{4}$$

with $h'$ the first radial derivative of the liquid height $h(r)$. The symbols used here, i.e., $\top$, $\cdot$, and $\otimes$, stand for the transposed matrix, the matrix product, and the tensor product, respectively. The surface operators are defined as follows:

$$\overline{\overline{\mathrm{grad}}}_\sigma(\mathbf{v}_\sigma) = \overline{\overline{\mathrm{grad}}}(\mathbf{v}_\sigma) \cdot \overline{\overline{P}}, \tag{5}$$

$$\mathrm{div}_\sigma(\mathbf{v}_\sigma) = \mathrm{Tr}[\overline{\overline{\mathrm{grad}}}(\mathbf{v}_\sigma) \cdot \overline{\overline{P}}]. \tag{6}$$

As explained above, only the surface shear viscosity $\eta_\sigma$ is solicited, with $\mathrm{div}_\sigma(\mathbf{v}_\sigma) = 0$. The surface stress tensor is then reduced to the shear and surface tension effects

$$\overline{\overline{T}}_\sigma = \gamma\overline{\overline{P}} + \eta_\sigma\overline{\overline{\tau}}_\sigma, \tag{7}$$

where $\overline{\overline{\tau}}_\sigma$ is the surface strain rate tensor, with the following non-null components:

$$\tau_{\sigma_{r\theta}} = \tau_{\sigma_{\theta r}} = \frac{1}{1 + h'^2}\left(\frac{\partial v_\sigma}{\partial r} - \frac{v_\sigma}{r} + h'\frac{\partial v_\sigma}{\partial z}\right), \tag{8}$$

$$\tau_{\sigma_{z\theta}} = \tau_{\sigma_{\theta z}} = \frac{h'}{1 + h'^2}\left(\frac{\partial v_\sigma}{\partial r} - \frac{v_\sigma}{r} + h'\frac{\partial v_\sigma}{\partial z}\right). \tag{9}$$

### 2. Jump momentum balance

The jump momentum balance, evaluated on a heterogeneous elementary volume overlapping the zero-thickness interface, is used to establish the relation between surface and volume stresses [23]

$$\mathbf{div}_\sigma(\overline{\overline{T}}_\sigma) + \mathbf{f}_\sigma = [\![\overline{\overline{T}} \cdot \mathbf{n}]\!]. \tag{10}$$

Here $\mathbf{f}_\sigma$ stands for a surface (in-excess) body force and is not considered in this study. The right-hand term corresponds to the jump in volumic stresses on both side of the interface, while the left-hand term is the surface divergence of the surface stress tensor, which is expressed using the double dot product:

$$\mathbf{div}_\sigma(\overline{\overline{T}}_\sigma) = \overline{\overline{\overline{\mathrm{grad}}}}(\overline{\overline{T}}_\sigma) : \overline{\overline{P}}. \tag{11}$$

The third-order tensor $\overline{\overline{\overline{\mathrm{grad}}}}(\overline{\overline{T}}_\sigma)$ can be broken down into three tensors of second order, detailed in Appendix A, such that the component along the direction $\mathbf{e_i}$ is

$$\mathbf{div}_\sigma(\overline{\overline{T}}_\sigma) \cdot \mathbf{e_i} = \mathrm{Tr}[\overline{\overline{P}} \cdot \overline{\overline{\mathrm{grad}}}_{e_i}(\overline{\overline{T}}_\sigma)]. \tag{12}$$

### 3. Interface shape

The vertical component of the JMB, involving surface tension and pressure effects, leads directly to the Laplace-Young equation, expressed in the cylindrical coordinate system

$$\frac{\gamma}{(1+h'^2)^{3/2}}\left(h'' + \frac{h'}{r} + \frac{h'^3}{r}\right) = \rho g h, \tag{13}$$

where $h'$ and $h''$ are, respectively, the first and second radial derivatives of liquid height $h(r)$. The contact angle $\phi$ is imposed on the two sidewalls of the annular viscometer by the following boundary condition:

$$h'|_{r_i} = -h'|_{r_o} = -\coth\phi. \tag{14}$$

### 4. Interface dynamics

The azimuthal component of the JMB takes into account the viscous effects of the interface and those of the subphase, with an additional term for the tangential gradient of surface viscosity and an additional term linked to surface curvature. Ignoring the dynamic viscosity of gas, we obtain

$$\underbrace{\eta_\sigma \frac{\partial}{\partial s}\left(\frac{1}{r}\frac{\partial(r v_\sigma)}{\partial s}\right)}_{\text{surface viscous shear}} + \underbrace{\frac{\partial\eta_\sigma}{\partial s}\left[r\frac{\partial}{\partial s}\left(\frac{v_\sigma}{r}\right)\right]}_{\text{surface nonuniformity}} + \underbrace{\eta_\sigma\,\frac{v_\sigma}{r}\frac{2h'h''}{(1+h'^2)^2}}_{\text{surface curvature}} = \underbrace{\eta r\frac{\partial}{\partial n}\left(\frac{v}{r}\right)\bigg|_{h(r)}}_{\text{bulk shear}}, \tag{15}$$

where the tangential and normal derivatives at the interface are defined as a function of the radial and vertical coordinates

$$\frac{\partial \cdot}{\partial s} = \frac{1}{\sqrt{1+h'^2}}\left(\frac{\partial \cdot}{\partial r} + h'\frac{\partial \cdot}{\partial z}\right), \tag{16}$$

$$\frac{\partial \cdot}{\partial n} = \frac{1}{\sqrt{1+h'^2}}\left(\frac{\partial \cdot}{\partial z} - h'\frac{\partial \cdot}{\partial r}\right). \tag{17}$$

A non-Newtonian behavior of the interface is taken into account mainly via the second term of Eq. (15) because it involves the emergence of a surface viscosity radial profile.

### C. Dimensionless quantities

The governing equations are normalized considering the following bulk and surface dimensionless quantities, denoted by an asterisk superscript: the radial coordinate $r^* = r/r_o$ (except in the figures where $r^* = (r - r_i)/(r_o - r_i)$); the vertical coordinate $z^* = z/h_0$, where $h_0$ is the mean depth of the annular channel; the azimuthal bulk velocity $v^* = v/r_o\Omega$; the curvilinear abscissa along the interface $s^* = s/r_0$; the normal coordinate at the interface $n^* = n/h_0$; and the azimuthal surface velocity $v_\sigma^* = v_\sigma/r_o\Omega$. A rheological dimensionless number can be put forward from the azimuthal component of the jump momentum balance. Called the Boussinesq number, it describes the competition between bulk and surface shear stresses

$$\text{Bo} = \epsilon\frac{\eta_\sigma}{\eta r_o}, \tag{18}$$

where $\epsilon = h_0/r_o$ stands for the vertical aspect ratio. Thus, the following normalized azimuthal component of the JMB is obtained:

$$\text{Bo}\,\frac{\partial}{\partial s^*}\left(\frac{1}{r^*}\frac{\partial r^* v_\sigma^*}{\partial s^*}\right) + \frac{\partial\,\text{Bo}}{\partial s^*}\left[r^*\frac{\partial}{\partial s^*}\left(\frac{v_\sigma^*}{r^*}\right)\right] + \text{Bo}\,\frac{v_\sigma^*}{r^*}\frac{2\epsilon^2 h'^* h''^*}{(1+\epsilon^2 h'^{2*})^2} = r^*\frac{\partial}{\partial n^*}\left(\frac{v^*}{r^*}\right)\bigg|_{h^*(r^*)}. \tag{19}$$
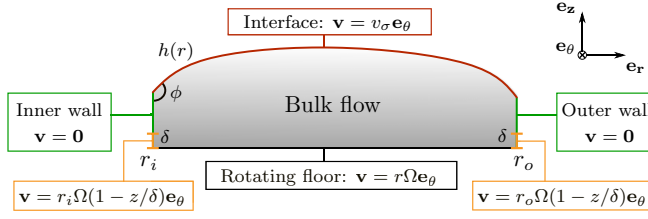
FIG. 3. Geometry and boundary conditions of the 2D axisymmetric model.

### D. Constitutive law for surface viscosity

A number of empirical models are available to describe the non-Newtonian behavior of a fluid body, such as those proposed by Ostwald, Ellis, Carreau, Cross and Williamson, and Powell and Eyring. To model the variations in surface shear viscosity with the tangent shear rate along the interface, denoted by $\tau_\sigma$, we have chosen to use here the Carreau model adapted to the case of a fluid interface (see also [29,30,36]):

$$\eta_{\sigma_c}(\tau_\sigma) = \eta_\sigma [1 + (\lambda\tau_\sigma)^2]^{(n-1)/2}. \tag{20}$$

This law, extensively used for its simplicity, allows the description of an interface exhibiting a constant (Newtonian) viscosity at a low shear rate, denoted by $\eta_\sigma$, and a power-law behavior for higher shear rates. The transition between these two evolutions is characterized by the relaxation time, denoted by $\lambda$. The power-law index, denoted by $n$, is used to describe a shear-thinning interface ($n < 1$) or a shear-thickening interface ($n > 1$). When the index equals 1, a Newtonian behavior is recovered. For the annular viscometer configuration, the shear rate along the interface is written as follows:

$$\tau_\sigma(r) = r\frac{\partial}{\partial s}\left(\frac{v_\sigma}{r}\right). \tag{21}$$

Thus, the Carreau constitutive model can be written as a function of the radius within the dimensionless form as follows:

$$\mathrm{Bo}_c(r^*) = \mathrm{Bo}\left\{1 + \left[\lambda\Omega r^*\frac{\partial}{\partial s^*}\left(\frac{v_\sigma^*(r^*)}{r^*}\right)\right]^2\right\}^{(n-1)/2}. \tag{22}$$

### E. Numerical implementation

Numerical simulations of the 2D axisymmetric model are solved by the finite-element method. The Stokes (elliptic) equation is implemented in weak formulation using the mathematical module dedicated to partial derivative equations in COMSOL software. The boundary conditions considered are presented in Fig. 3.

A no-slip boundary condition is applied along the sidewalls, except in the vicinity of the floor, rotating at $\Omega$ speed, to take account of the presence of a lubrication gap in the experimental conditions and incidentally to avoid a singularity on the Dirichlet boundary conditions. Thus, a Couette profile is introduced for the velocity azimuthal component along two small vertical segments of height $\delta$ such that $\delta \ll h$. The value $\delta = 0.5$ mm is compliant with the majority of experimental conditions for which it is necessary to respect lubrication between the rotating floor and the static vertical walls. For the inner and the outer radii, the following boundary conditions are thus imposed:

$$v(r = r_i, z) = \begin{cases} r_i\Omega\left(1 - \frac{z}{\delta}\right) & \text{for } z \in [0, \delta] \\ 0 & \text{for } z \in [\delta, h(r_i)], \end{cases} \tag{23}$$

$$v(r = r_o, z) = \begin{cases} r_o\Omega\left(1 - \frac{z}{\delta}\right) & \text{for } z \in [0, \delta] \\ 0 & \text{for } z \in [\delta, h(r_o)]. \end{cases} \tag{24}$$

Regarding the liquid-gas boundary condition, the interface shape and the surface velocity dynamics are given by the surface rheology equations and the associated JMB which are solved through their corresponding weak formulations. The vertical component of the JMB, equivalent to the Laplace-Young equation, is implemented in a 1D axisymmetric model, separately from the flow equations. Indeed, as previously stated, the annular flow is considered not to modify the interface shape. The weak formulation is then obtained by multiplying Eq. (13) by the test function $\omega_z$ and then by integrating it along the radial direction. Applying integration by parts and considering the term

$$\alpha = \left[ 1 + \left( \frac{dz}{dr} \right)^2 \right]^{3/2} \qquad (25)$$

as a relaxation parameter, the following weak formulation is resolved:

$$\int_0^r \left\{ \frac{d\omega_z}{dr} \frac{dz}{dr} - \omega_z \left[ \frac{1}{r} \frac{dz}{dr} + \frac{1}{r} \left( \frac{dz}{dr} \right)^3 - \alpha \frac{z}{l_c^2} \right] \right\} dr = 0. \qquad (26)$$

The computational domain consists of a line of width $r_o - r_i$, discretized in small segments. The contact angle is imposed at the sidewalls via an end-point boundary condition of Neumann type [see Eq. (14)]. Resolution of this independent model yields the height of the interface, denoted hereafter by $h(r)$, as a function of the capillary length, contact angle, and aspect ratios.

For the interface dynamics, the azimuthal component is directly implemented as a boundary condition along the liquid-gas interface in the 2D axisymmetric model (see Fig. 3). As above, the weak formulation is obtained by multiplying Eq. (15) by the test function, denoted by $\omega_{v_\sigma}$, and then integrating it along the curvilinear abscissa $s$. Integration by parts of the second term of Eq. (15) allows us to simplify the formulation by lowering derivative order and eliminating the tangential derivative of the surface viscosity profile:

$$\int_0^s \left\{ \eta_\sigma \frac{\partial \omega_{v_\sigma}}{\partial s} \left[ r \frac{\partial}{\partial s} \left( \frac{v_\sigma}{r} \right) \right] - 2\eta_\sigma \frac{\omega_{v_\sigma}}{\sqrt{1 + h'^2}} \frac{\partial}{\partial s} \left( \frac{v_\sigma}{r} \right) + \eta \omega_{v_\sigma} \left[ r \frac{\partial}{\partial n} \left( \frac{v}{r} \right) \right] \right\} ds = 0. \qquad (27)$$

The computational domain consists of triangular elements with a refinement at the free surface. When the interface is Newtonian, a direct (linear) steady-state solver suffices to resolve the problem (multifrontal massively parallel sparse direct solver and use of lower-upper factorization [37]). To allow for the non-Newtonian behavior of the interface, a relaxation method (iterative) is required such that the viscosity $\eta_{\sigma_c}$ is corrected at each iteration $i$ as a function of the shear rate calculated at the previous iteration $i - 1$.

## IV. RESULTS AND INTERPRETATIONS

### A. Benchmark: Newtonian planar interface

First, model implementation is validated by comparing the surface variables obtained by numerical simulations, with Mannheimer and Schechter's analytical solution [13]. Consequently, the case of a planar interface ($\phi = 90°$) with a Newtonian behavior ($n = 1$) is considered. The analytical solution, recalled in Appendix B, is calculated for the annular viscometer configuration presented earlier ($r_i/r_o = 30/70$ and $\epsilon = 10/70$).

As shown in Fig. 4, the surface velocity, surface shear, and normal bulk shear at the interface are in perfect agreement for the different Boussinesq values considered. The numerical study proposed in this paper thus yields results that are similar to Mannheimer and Schechter's analytical solution when the interface is planar and Newtonian.

In this specific case, as long as inertial effects remain negligible, the normalized velocity profile along the interface only depends on the Boussinesq number. Then measurement of the surface velocity field allows us to directly identify the surface shear viscosity by comparison with the
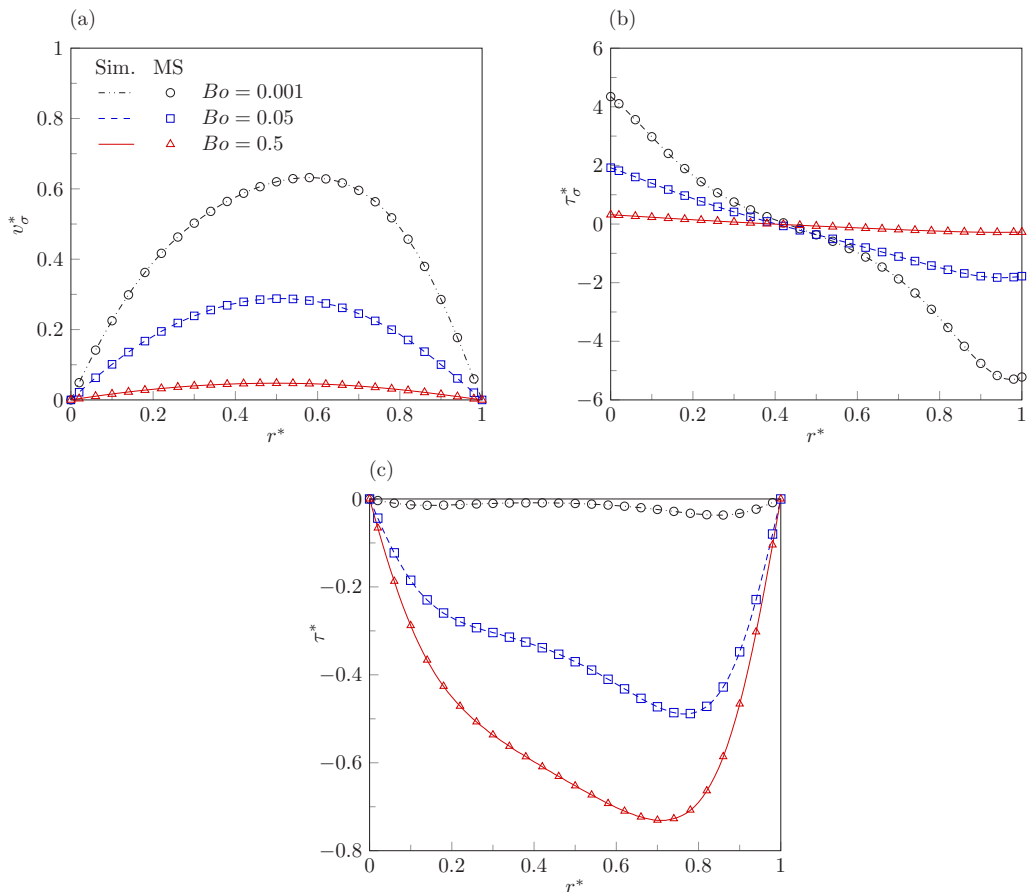
FIG. 4. (a) Surface velocity profile, (b) surface shear, and (c) bulk shear at the interface obtained by numerical simulations and compared to the analytical solution of Mannheimer and Schechter for various Boussinesq numbers ($n = 1$ and $\phi = 90°$).

analytical or numerical solution. Moreover, a simple way of checking experimentally the Newtonian behavior of an interface is to carry out a series of tests at different rotation speeds, and so, at different (but small enough) Reynolds numbers. The normalized velocity profiles are supposed to be superimposed perfectly. Otherwise, the interface is probably non-Newtonian and the resulting velocity profiles evolution can be used to characterize the mechanical behavior of the interface.

## B. Non-Newtonian planar interface

In this section the interface is considered to be planar, but now with a non-Newtonian behavior, either of the shear-thinning type ($n = 0.5$) or of the shear-thickening type ($n = 2$). According to the Carreau model (20), the surface shear viscosity $\eta_{\sigma_c}$ depends on the (tangential) surface shear $\tau_\sigma$; the constant (Newtonian) surface shear viscosity $\eta_\sigma$, which is related to the classical (Newtonian) Boussinesq number; and the relaxation time $\lambda$. To evaluate the changes due to a non-Newtonian interface, the respective influence of these parameters is assessed independently of each other, on the surface variables and the bulk shear at the interface (Fig. 5), by comparing them to the Newtonian reference case.
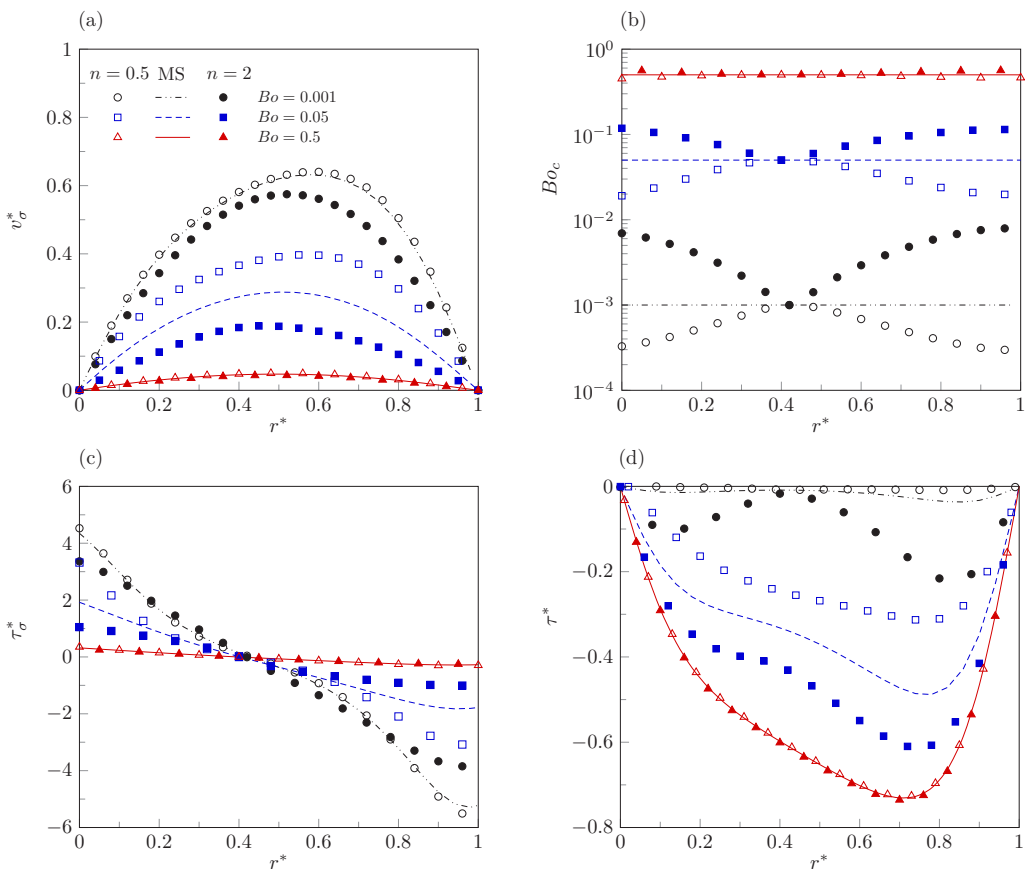
FIG. 5. (a) Surface velocity profile, (b) Boussinesq number along the interface, (c) surface shear, and (d) bulk shear at the interface for the Newtonian (MS), shear-thinning ($n = 0.5$), and shear-thickening ($n = 2$) cases for various (Newtonian) Boussinesq numbers (Re = 100, $\lambda = 100$, and $\phi = 90°$).

### 1. Influence of behavior type

When the power-law index $n$ is less than 1, interface behavior is of the shear-thinning type. Consequently, surface viscosity decreases in the zones where the interface exhibits a high shear, namely, close to the fixed sidewalls [see Fig. 4(b)]. As there are fewer viscous dissipations, the surface velocity, shown in Fig. 5(a) with open symbols, tends to be higher than in the equivalent Newtonian case.

In contrast, a shear-thickening behavior corresponds to a power-law index greater than 1. In this case, surface viscosity increases close to the sidewalls and the interfacial strain rate is less intense. The velocity at the interface [closed symbols in Fig. 5(a)] is then lower than in the equivalent Newtonian case.

Finally, the velocity profile observed is slightly deformed at the outer part of the annular channel for both types of behavior. This is due to a shear asymmetry along the interface, which is more intense in the outer part of the viscometer [see Fig. 4(b)]. Variations in surface viscosities are thus more intense in this zone with greater shear-thinning or shear-thickening effects [Fig. 5(b)].

### 2. Influence of Boussinesq number

The (Newtonian) Boussinesq number conditions the value of surface viscosity at the point where surface shear is canceled out, positioned more or less at the center of the annular channel. It also
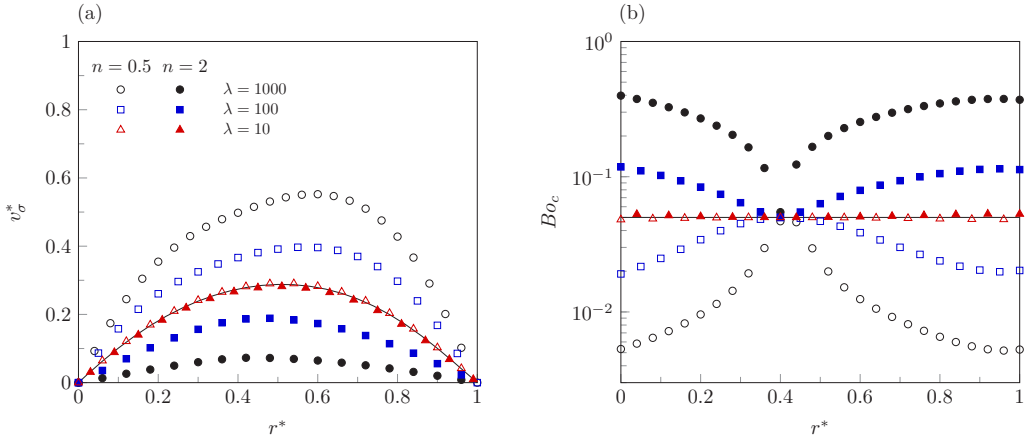
FIG. 6. (a) Surface velocity profile and (b) Boussinesq number along the interface for the Newtonian (black solid curve), shear-thinning ($n = 0.5$), and shear-thickening ($n = 2$) cases for various relaxation times $\lambda$ (Re = 100, Bo = 0.05, and $\phi = 90°$).

affects the tangential shear range of the interface. For high values of the Boussinesq number, typically Bo = 0.5, the surface velocity is very low and so the interfacial strain rate is very restricted, implying an almost constant viscosity. All surface quantities along a shear-thinning or shear-thickening interface are then very close to those obtained for the Newtonian case [Fig. 5(b)].

In contrast, a small Boussinesq number, such that Bo = 0.001, leads to a large variation in surface viscosity due to intense surface shear [Fig. 5(c)]. Consequently, the velocity of a shear-thickening interface decreases significantly compared to the Newtonian case. However, the velocity profile along the shear-thinning interface remains virtually unchanged as it logically tends to the maximum velocity obtained when the free surface is noncontaminated.

The intermediate case, corresponding to Bo = 0.05, is the case presenting the greatest impact on surface flow. Tangent shear at the interface is sufficient to cause large variations in surface viscosity, without however obtaining the maximum velocity profile for the shear-thinning case (see the case of a liquid surface free of contamination).

### 3. Influence of relaxation time

The relaxation time $\lambda$ defines the transition between the Newtonian behavior observed at low surface shear and the power law for higher interfacial strain rates. For a sufficiently low value, typically $\lambda = 10$, the velocity profile along the interface is almost identical to that of a Newtonian surface flow [see Fig. 6(a)]. In this case, the maximum tangential shear undergone by the interface is less than the relaxation shear, defined by $\tau_{\sigma_c} = 1/\lambda$. In other words, the interface is not sufficiently solicited to reveal its non-Newtonian behavior. Conversely, a large value of the relaxation time reduces the critical shear from which non-Newtonian behavior arises. Surface viscosity variations become much more significant, as shown in Fig. 6(b) for $\lambda = 100$ and $\lambda = 1000$, and the surface velocity profiles are accordingly modified [Fig. 6(a)].

### C. Role of interface curvature

The impact of a curved interface is evaluated by considering mass conservation and two different cases: Either the channel is filled with an aqueous solution whose interface is populated by adsorbed molecules or it is filled with molten aluminium covered by an oxide film. Both cases are interesting to investigate as they exhibit different capillary lengths: $l_c \sim 2$ mm for an aqueous solution and
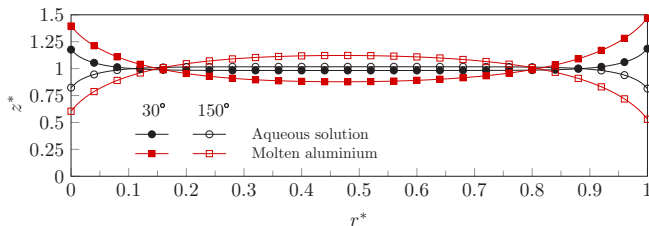
FIG. 7. Evolution of the bath height for an aqueous solution ($l_c = 2$ mm) and molten aluminium ($l_c = 6$ mm) for various contact angles.

$l_c \sim 6$ mm for molten aluminium. The shape of their interface is thus significantly different for the same contact angle imposed at the sidewalls of the viscometer.

Figure 7 shows the evolution of bath height for various contact angles: $\phi = 30°$ for the wetting case, $\phi = 150°$ for the nonwetting case, and naturally $\phi = 90°$ when the interface is planar. As explained earlier, the shape of the surface is determined by resolving the Laplace-Young equation. The subphase height is then adjusted by mass conservation.

### 1. Newtonian curved interface

We first examine the case where the curved interface has a Newtonian behavior. Surface velocity profiles of the wetting and nonwetting cases are compared to the profile obtained when the interface is planar for various Boussinesq numbers. Figure 8(a) allows us to verify that the interface shape does not significantly modify the surface velocity profile in the case of an aqueous solution whatever the value of the contact angle. The hypothesis of a planar interface is thus valid for the shallow-channel surface viscometer, whose capillary length to channel width ratio is 0.05. However, the interface curvature can have a significant effect, even with an aqueous phase [14], especially for the deep-channel viscometer layout.

Conversely, interface shape significantly impacts the surface velocity field in the case of molten aluminium, where differences from the planar case increase as the Boussinesq number decreases. When $\phi = 30°$, a dead zone appears close to the fixed sidewalls (see Fig. 9) with a lower surface velocity than for the planar case. In this zone, surface shear drops to practically reach a null value at the triple line [see Fig. 8(c)]. In contrast, the nonwetting case leads to an increase in surface velocity at the far ends of the channel and thus to a very intense tangent shear at the interface. For high-Boussinesq-number values, typically Bo = 0.5, velocity profiles and surface shear [Fig. 8(d)] are virtually identical, as viscous dissipation along the interface prevails over entrainment of the subphase.

### 2. Non-Newtonian curved interface

In light of the above observations, interface curvature must mainly be considered for the case of weakly oxidized liquid metals. The nonwetting case is of particular interest as it implies a high surface shear at the triple line, unlike the wetting case. This is why Fig. 10 only shows velocity profiles along a non-Newtonian interface for the case of a molten aluminium bath with $\phi = 150°$ and $\phi = 90°$.

As expected, interface curvature tends to amplify the shear-thinning and shear-thickening effects, in particular close to the sidewalls with more intense viscosity variations. With a high capillary length and a contact angle close to $\phi = 180°$, there is a marked increase in the surface shear range compared to the planar case. In other words, a curved interface enhances detection of a non-Newtonian behavior due to larger viscosity variations.
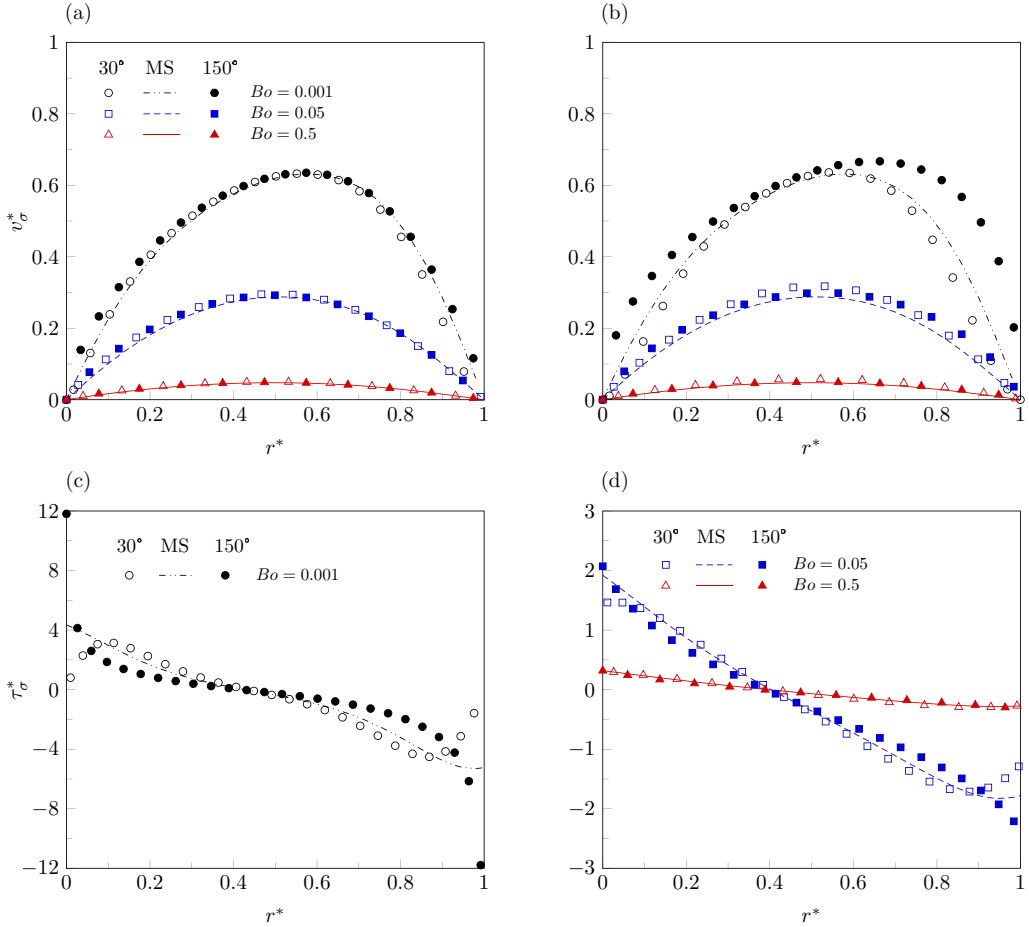
FIG. 8. (a) and (b) Surface velocity profile and (c) and (d) surface shear along a Newtonian interface ($n = 1$), for the wetting ($\phi = 30°$), planar (MS), and nonwetting ($\phi = 150°$) cases, as a function of the Boussinesq number and the liquid bath: (a) an aqueous solution ($l_c = 2$ mm) or (b)–(d) molten aluminium ($l_c = 6$ mm).

## D. Measuring range of the annular viscometer

In this section, the detection limits of the annular viscometer is discussed, with the Boussinesq number range likely to be measured and notably the possibility of revealing a non-Newtonian behavior, considering both a planar and a curved interface.
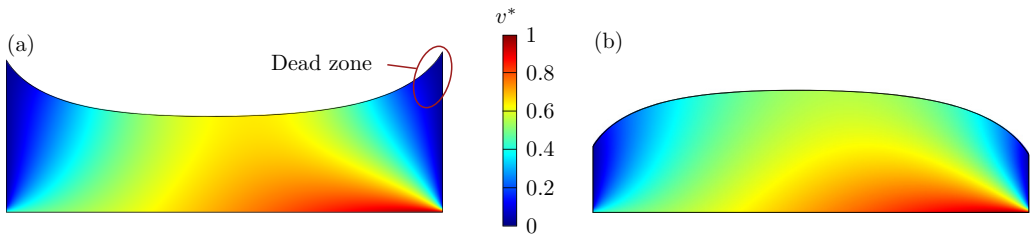


FIG. 9. Bulk velocity field for (a) the wetting case ($\phi = 30°$) and (b) the nonwetting case ($\phi = 150°$), considering the molten aluminium subphase ($l_c = 6$ mm) with Bo = 0.001.
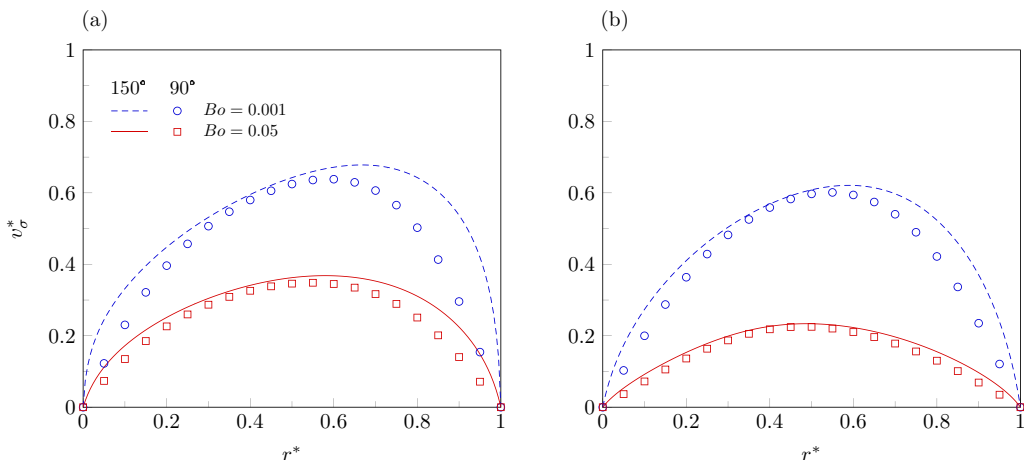
FIG. 10. Surface velocity profile for (a) a shear-thinning ($n = 0.5$) and (b) a shear-thickening ($n = 2$) interface for various Boussinesq number and contact angle, considering the molten aluminium subphase ($l_c = 6$ mm, $\lambda = 100$, and Re $= 100$).

With respect to the first point, the maximum value of the surface velocity max($v_\sigma^*$) is determined as a function of the Boussinesq number for an aqueous solution, considering a Newtonian interface [black curve in Fig. 11(a)]. As the surface shear viscosity is identified from the surface velocity profile, the latter must necessarily be different from the profile obtained for a (noncontaminated) free surface. Consequently, below a Boussinesq number of $10^{-3}$ ($\eta_\sigma = 10^{-7}$ kg s$^{-1}$), surface flow is less and less sensitive to the presence of residual contamination. The upper detection limit corresponds to the case where the interface is virtually motionless (intense contamination), which is roughly equivalent to a Boussinesq number of approximately unit order ($\eta_\sigma = 10^{-4}$ kg s$^{-1}$). Then the measurement range of the shallow-channel surface viscometer covers three orders of magnitude: $10^{-3} <$ Bo $< 1$.
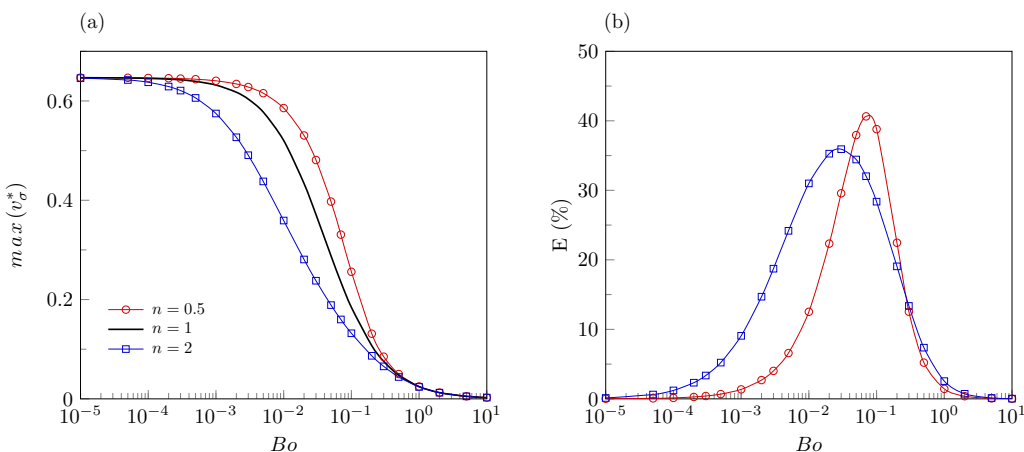


FIG. 11. (a) Maximum surface velocity along the interface for the shear-thinning ($n = 0.5$), Newtonian ($n = 1$), and shear-thickening ($n = 2$) cases as a function of the Boussinesq number. (b) Relative difference between the Newtonian and the non-Newtonian cases. Here $\phi = 90°$, $\lambda = 100$, and Re $= 100$.
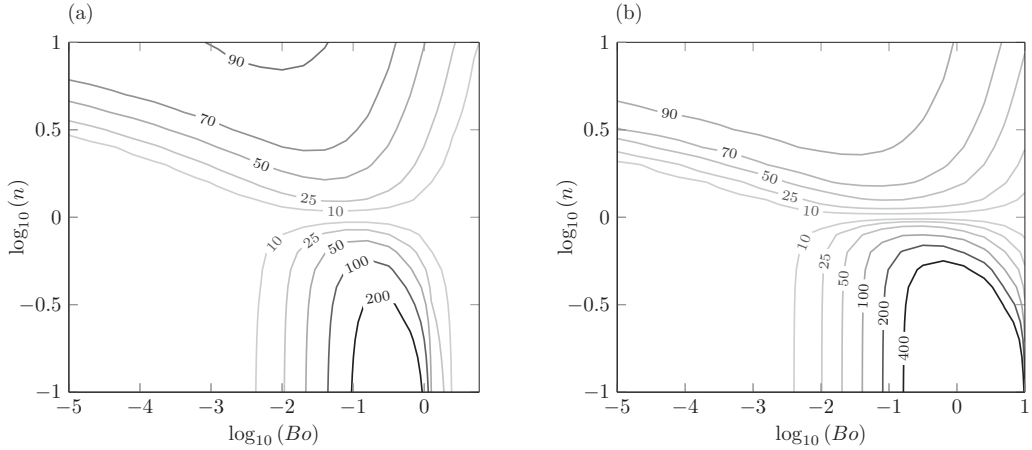
FIG. 12. Isovalues of the relative difference $E$ (%), as a function of the Boussinesq number and the power-law index $n$ for (a) $\lambda = 200$ and (b) $\lambda = 2000$, with $\phi = 90°$ and Re $= 200$.

### 1. Sensitivity to non-Newtonian behavior

To assess the ability of the annular viscometer to highlight a non-Newtonian behavior, the maximum value of the surface velocity is also determined for the shear-thinning ($n = 0.5$) and shear-thickening ($n = 2$) cases, with $\lambda = 100$ and Re $= 100$ [Fig. 11(a)]. The relative difference, denoted by $E$ (%), is calculated between the non-Newtonian case ($n \neq 1$) and the Newtonian case ($n = 1$), the latter being taken as the reference case:

$$E \ (\%) = 100 \times \left| \frac{\max(v_\sigma^*)_{n \neq 1} - \max(v_\sigma^*)_{n=1}}{\max(v_\sigma^*)_{n=1}} \right|.$$

Figure 11(b) highlights an increased sensitivity to a non-Newtonian behavior around the specific value of the Boussinesq number which corresponds to the peak of the curves. When the interface is shear thinning, a Boussinesq number around the value 0.07 generates a relative difference of roughly 40%. In other words, the velocity of a shear-thinning interface will be 40% higher than that of the associated Newtonian case (for Bo $= 0.07$, $\lambda = 100$, and Re $= 100$), which makes easier the detection of a non-Newtonian behavior. A similar comment can be made on shear-thickening behavior, with an important relative difference of 35% around the specific value of the Boussinesq number of 0.03. However, a major difference appears regarding the detection range: A shear-thickening behavior can be made evident on a wider range of the Boussinesq number than in the shear-thinning case, especially for a weakly contaminated surface.

The investigation of the sensitivity of channel viscometry to a non-Newtonian behavior also requires us to focus on the role of the power-law index $n$. The relative difference $E$ (%) is also determined as a function of the Boussinesq number, for a power-law index $n$ ranging between 0.1 and 10, and two different values of the relaxation time $\lambda$ [see the isovalues of $E$ (%) in Fig. 12]. Doing this, it is possible to visualize the areas where the relative difference is larger than 10%. Not surprisingly, it is easy to demonstrate a non-Newtonian behavior when the power-law index is far enough from unity. In a similar way, an interface characterized by a high value of the relaxation time consistently enhances a non-Newtonian behavior.

### 2. Focus on the role of surface curvature

Now, in order to assess how the contact angle can highlight the non-Newtonian behavior, the molten aluminium is considered. Figure 13, showing the relative difference between the Newtonian and the non-Newtonian cases for various contact angles, allows us to confirm the
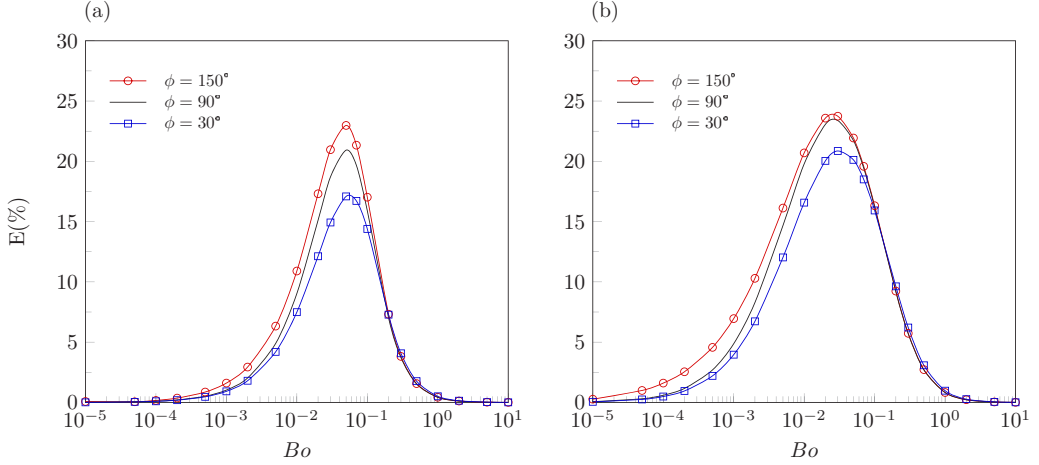
FIG. 13. Relative difference of the maximum surface velocities between the Newtonian and the non-Newtonian cases, with (a) a shear-thickening interface ($n = 0.5$) and (b) a shear-thinning interface ($n = 2$), for various contact angles considering molten aluminium ($l_c = 6$ mm, Re $= 100$, and $\lambda = 100$).

previous observations. Indeed, the nonwetting case tends to amplify non-Newtonian effects with higher sensitivity, more particularly at a low value of the Boussinesq number. The wetting case has the opposite effect due to an overall decrease in surface shear. Therefore, a nonwetting contact angle may appropriately be used for a better detection of a non-Newtonian behavior.

### 3. Identification procedure of the surface shear viscosity

Finally, from an experimental point of view, it is sufficient to perform tests under different rotation speeds in order to evaluate the parameters involved in the surface viscosity model. To demonstrate this, Fig. 14(a) shows the evolution of the surface velocity profiles with the Reynolds number for a shear-thinning ($n = 0.5$) and a shear-thickening ($n = 2$) interface.
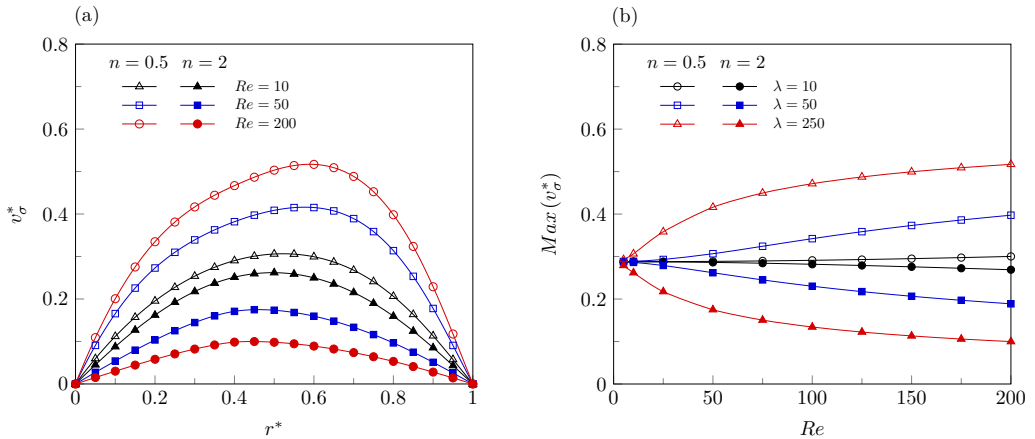


FIG. 14. (a) Dependence of the surface velocity profiles on the Reynolds number for a shear-thinning ($n = 0.5$) and a shear-thickening ($n = 2$) interface, with Bo $= 0.05$ and $\lambda = 250$. (b) Dependence of the maximum surface velocity on the Reynolds number, with Bo $= 0.05$.

An experiment conducted at a low rotation speed (small Reynolds number) makes it possible to approach the constant (Newtonian) surface viscosity value due to a very restricted surface shear. In this way, surface viscosity is (almost) constant all along the interface and the velocity profile approaches the Newtonian case. Then, by progressively increasing the rotation speed, but not beyond a large enough Reynolds number for which the inertia effect could become significant, the non-Newtonian behavior of the interface can be made evident from a growing surface shear. By considering the dimensionless surface velocity along the interface, it is possible to define its maximum value $\max(v_\sigma^*)$ as a new variable. Thereby, a significant dependence of the latter on the Reynolds number [Fig. 14(b)] delivers most useful information on the non-Newtonian behavior of the interface. A comparison between experimental data and numerical simulations based on the plot $\max(v_\sigma^*) = f(\mathrm{Re})$ is revealed to be decisive for solving the inverse problem since it allows for a quick identification of the Boussinesq number, the power-law index, and the relaxation time.

## V. CONCLUSION

Taking into account surface curvature effects is a priority in surface rheology because they can be revealed to be a serious source of experimental errors whenever the surface viscosities are identified with the assumption that the liquid surface remains planar. This is true whatever the rheological method developed, either based on channel viscosimetry or based on the drag measurement of moving actuators straddling the liquid surface [26,38].

The numerical study conducted in this paper enabled assessment of the two-way coupling between a non-Newtonian, possibly non-Euclidean (curved), interface and a supporting flow in the configuration of the annular channel viscometer. To this end, the Boussinesq-Scriven law model was enhanced by a Carreau-law model, for which surface shear viscosity depends on the strain rate along the interface. The interfacial jump momentum balance was also written here so as to take into account surface curvature effects and further developed according to a weak formulation prior to its resolution by the finite-element method.

After having validated the implementation of the numerical model by comparing the results with Mannheimer and Schechter's analytical solution valid for the case of a Newtonian planar interface, the influence and the measurement range of the parameters involved in the Carreau model have been evaluated. It has been proved that a series of experiments conducted at different rotation speeds can determine the three parameters characterizing the non-Newtonian behavior of a contaminated liquid surface, namely, the Boussinesq number, the power-law index, and the relaxation time.

The influence of surface curvature on the flow of a non-Newtonian interface was also demonstrated with a notable benefit in a nonwetting case, particularly for a significant capillary length to channel width ratio. Finally, it was found that a shallow-channel configuration is particularly well suited to developing the mechanical characterization of a non-Newtonian interface submitted to shear thinning or shear thickening.

Among possible prospects for the present paper, one would consist in studying the additional role of the Reynolds number: The aim would be to widen the measurement range of the surface shear viscosity, to identify the surface dilatational viscosity in more realistic conditions (wetting effects included), and finally to investigate the sensitivity of the latter viscosity to a non-Newtonian behavior.

## APPENDIX A: GRADIENT OF A SECOND-ORDER TENSOR

The stress tensor gradient $\overline{\overline{\overline{T}}}_\sigma$ can be broken down into three second-order tensors (considering $\partial \cdot /\partial\theta = 0$), which are easier to handle:

$$\overline{\overline{\mathrm{grad}}}_{e_r}(\overline{\overline{T}}_\sigma) = \begin{bmatrix} \dfrac{\partial T_{\sigma rr}}{\partial r} & \dfrac{\partial T_{\sigma r\theta}}{\partial r} & \dfrac{\partial T_{\sigma rz}}{\partial r} \\[2ex] \dfrac{-T_{\sigma r\theta}-T_{\sigma\theta r}}{r} & \dfrac{T_{\sigma rr}-T_{\sigma\theta\theta}}{r} & \dfrac{-T_{\sigma\theta z}}{r} \\[2ex] \dfrac{\partial T_{\sigma rr}}{\partial z} & \dfrac{\partial T_{\sigma r\theta}}{\partial z} & \dfrac{\partial T_{\sigma rz}}{\partial z} \end{bmatrix},$$

$$\overline{\overline{\mathrm{grad}}}_{e_\theta}(\overline{\overline{T}}_\sigma) = \begin{bmatrix} \dfrac{\partial T_{\sigma\theta r}}{\partial r} & \dfrac{\partial T_{\sigma\theta\theta}}{\partial r} & \dfrac{\partial T_{\sigma\theta z}}{\partial r} \\[2ex] \dfrac{T_{\sigma rr}-T_{\sigma\theta\theta}}{r} & \dfrac{T_{\sigma r\theta}+T_{\sigma\theta r}}{r} & \dfrac{T_{\sigma rz}}{r} \\[2ex] \dfrac{\partial T_{\sigma\theta r}}{\partial z} & \dfrac{\partial T_{\sigma\theta\theta}}{\partial z} & \dfrac{\partial T_{\sigma\theta z}}{\partial z} \end{bmatrix},$$

$$\overline{\overline{\mathrm{grad}}}_{e_z}(\overline{\overline{T}}_\sigma) = \begin{bmatrix} \dfrac{\partial T_{\sigma zr}}{\partial r} & \dfrac{\partial T_{\sigma z\theta}}{\partial r} & \dfrac{\partial T_{\sigma zz}}{\partial r} \\[2ex] \dfrac{-T_{\sigma z\theta}}{r} & \dfrac{T_{\sigma zr}}{r} & 0 \\[2ex] \dfrac{\partial T_{\sigma zr}}{\partial z} & \dfrac{\partial T_{\sigma z\theta}}{\partial z} & \dfrac{\partial T_{\sigma zz}}{\partial z} \end{bmatrix}.$$

## APPENDIX B: MANNHEIMER AND SCHECHTER'S SOLUTION

The analytical expression of the velocity profile along the interface assessed by Mannheimer and Schechter's solution [13] is

$$v_{\sigma_\theta}^* = \frac{2}{\frac{r_o}{e}} \sum_{i=1}^{\infty} \left\{ \frac{\left[\left(\frac{r_o}{e}\right)^2 \psi_0\left(\frac{r_o}{e}\beta_i\right) - \left(\frac{r_i}{e}\right)^2 \psi_0\left(\frac{r_i}{e}\beta_i\right)\right]}{\beta_i\left[\left(\frac{r_i}{e}\right)^2 \psi_0^2\left(\frac{r_i}{e}\beta_i\right) - \left(\frac{r_o}{e}\right)^2 \psi_0^2\left(\frac{r_o}{e}\beta_i\right)\right]} \frac{\psi_1\left(\frac{r}{e}\beta_i\right)}{\left[\cosh\left(\beta_i\frac{h}{e}\right) + \beta_i\frac{\eta_\sigma}{\eta e}\sinh\left(\beta_i\frac{h}{e}\right)\right]} \right\}, \quad \text{(B1)}$$

with

$$v_{\sigma_\theta}^* = \frac{v_{\sigma_\theta}}{r_o\Omega}, \quad \psi_0\left(\frac{r}{e}\beta_i\right) = J_0\left(\frac{r}{e}\beta_i\right)Y_1\left(\frac{r_i}{e}\beta_i\right) - J_1\left(\frac{r_i}{e}\beta_i\right)Y_0\left(\frac{r}{e}\beta_i\right),$$

and

$$\psi_1\left(\frac{r}{e}\beta_i\right) = J_1\left(\frac{r}{e}\beta_i\right)Y_1\left(\frac{r_i}{e}\beta_i\right) - J_1\left(\frac{r_i}{e}\beta_i\right)Y_1\left(\frac{r}{e}\beta_i\right).$$

The quantities $J$ and $Y$ stand for the first- and second-order Bessel functions with the associated indices 0 and 1. The channel width $r_o - r_i$ is denoted by $e$, while $\beta_i$ stands for the $i$th solution of the relation

$$J_1\left(\frac{r_o}{e}\beta_i\right)Y_1\left(\frac{r_i}{e}\beta_i\right) - J_1\left(\frac{r_i}{e}\beta_i\right)Y_1\left(\frac{r_o}{e}\beta_i\right).$$

Finally, the analytical expression of the subphase velocity is

$$v_\theta^* = \sum_{i=1}^{\infty} \left[A_i \sinh\left(\frac{\beta_i z}{e}\right) + B_i \cosh\left(\frac{\beta_i z}{e}\right)\right] \psi_1\left(\frac{\beta_i r}{e}\right), \quad \text{(B2)}$$

with

$$A_i = \frac{-B_i\left[\frac{\beta_i\eta_o}{\eta e}\cosh\left(\frac{\beta_i h}{e}\right) + \sinh\left(\frac{\beta_i h}{e}\right)\right]}{\frac{\beta_i\eta_o}{\eta e}\sinh\left(\frac{\beta_i h}{e}\right) + \cosh\left(\frac{\beta_i h}{e}\right)} \tag{B3}$$

and

$$B_i = \frac{2}{\frac{r_o}{e}} \frac{\left(\frac{r_o}{e}\right)^2 \psi_0\left(\frac{\beta_i r_o}{e}\right) - \left(\frac{r_i}{e}\right)^2 \psi_0\left(\frac{\beta_i r_i}{e}\right)}{\beta_i\left[\left(\frac{r_i}{e}\right)^2 \psi_0^2\left(\frac{\beta_i r_i}{e}\right) - \left(\frac{r_o}{e}\right)^2 \psi_0^2\left(\frac{\beta_i r_o}{e}\right)\right]}. \tag{B4}$$

[1] J. C. Slattery, *Interfacial Transport Phenomena* (Springer, Berlin, 1990).

[2] J. E. Young, D. Posada, J. M. Lopez, and A. H. Hirsa, Flow-induced 2D protein crystallization: Characterization of the coupled interfacial and bulk flows, Soft Matter **11**, 3618 (2015).

[3] S. A. McBride, S. P. Sanford, J. M. Lopez, and A. H. Hirsa, Shear-induced amyloid fibrillization: The role of inertia, Soft Matter **12**, 3461 (2016).

[4] V. S. Balaraj, P. C. H. Zeng, S. P. Sanford, S. A. McBride, A. Raghunandan, J. M. Lopez, and A. H. Hirsa, Surface shear viscosity as a macroscopic probe of amyloid fibril formation at a fluid interface, Soft Matter **13**, 1780 (2017).

[5] D. Langevin, Influence of interfacial rheology on foam and emulsion properties, Adv. Colloid Interface Sci. **88**, 209 (2000).

[6] E. Dickinson, Milk protein interfacial layers and the relationship to emulsion stability and rheology, Colloids Surf. B **20**, 197 (2001).

[7] M. Stoffel, S. Wahl, E. Lorenceau, R. Höhler, B. Mercier, and D. E. Angelescu, Bubble Production Mechanism in a Microfluidic Foam Generator, Phys. Rev. Lett. **108**, 198302 (2012).

[8] J. Wang, A. V. Nguyen, and S. Farrokhpay, Effects of surface rheology and surface potential on foam stability, Colloids Surf. A **488**, 70 (2016).

[9] J. Delacroix and L. Davoust, Electrical activity of the Hartmann layers relative to surface viscous shearing in an annular magnetohydrodynamic flow, Phys. Fluids **26**, 037102 (2014).

[10] J. Delacroix, L. Davoust, and K. Patouillet, Low Rm magnetohydrodynamics as a means of measuring the surface shear viscosity of a liquid metal: A first attempt on Galinstan, Rev. Sci. Instrum. **89**, 015103 (2018).

[11] E. Guzmán, J. Tajuelo, J. M. Pastor, M. A. Rubio, F. Ortega, and R. G. Rubio, Shear rheology of fluid interfaces: Closing the gap between macro- and micro-rheology, Curr. Opin. Colloid Interface Sci. **37**, 33 (2018).

[12] W. D. Harkins and R. J. Meyers, Viscosity of monomolecular films, Nature (London) **140**, 465 (1937).

[13] R. J. Mannheimer and R. S. Schechter, An improved apparatus and analysis for surface rheological measurements, J. Colloid Interface Sci. **32**, 195 (1970).

[14] A. J. Pintar, A. B. Israel, and D. T. Wasan, Interfacial shear viscosity phenomena in solutions of macromolecules, J. Colloid Interface Sci. **37**, 52 (1970).

[15] A. H. Hirsa, J. M. Lopez, and R. Miraghaie, Determination of surface shear viscosity via deep-channel flow with inertia, J. Fluid Mech. **470**, 135 (2002).

[16] L. Drazek, J.-F. Legrand, and L. Davoust, A first attempt to enhance the 2-D single-crystal growth of a protein at an air/water interface from hydrodynamics, J. Cryst. Growth **275**, e1467 (2005).

[17] L. Davoust, J.-L. Achard, and L. Drazek, Low-to-moderate Reynolds number swirling flow in an annular channel with a rotating end wall, Phys. Rev. E **91**, 023019 (2015).

[18] J. M. Lopez and A. H. Hirsa, Direct determination of the dependence of the surface shear and dilatational viscosities on the thermodynamic state of the interface: Theoretical foundations, J. Colloid Interface Sci. **206**, 231 (1998).

[19] J. Delacroix and L. Davoust, On the role of surface rheology in a magnetohydrodynamic swirling flow, Phys. Fluids **27**, 062104 (2015).

[20] A. H. Hirsa, J. M. Lopez, and R. Miraghaie, Measurement and computation of hydrodynamic coupling at an air/water interface with an insoluble monolayer, J. Fluid Mech. **443**, 271 (2001).

[21] L. Davoust, Y. L. Huang, and S.-H. Chang, Shearing of a stratified layer of amphiphilic (bio)molecules, Surf. Sci. **603**, 2777 (2009).

[22] D. A. Edwards, H. Brenner, and B. T. Wasan, *Interfacial Transport Processes and Rheology*, 1st ed. (Butterworth-Heinemann, Boston, 1991).

[23] R. Aris, *Vectors, Tensors and the Basic Equations of Fluid Mechanics* (Courier, Chelmsford, 1990.

[24] M. Joly, Non-Newtonian surface viscosity, J. Colloid Sci. **11**, 519 (1956).

[25] G. S. Patil, S. S. Katti, and A. B. Biswas, Surface viscosity of monomolecular films of *n*-long chain alcohols at various temperatures and pressures, J. Colloid Interface Sci. **25**, 462 (1967).

[26] P. Erni, P. Fischer, and E. J. Windhab, Stress- and strain-controlled measurements of interfacial shear viscosity and viscoelasticity at liquid/liquid and gas/liquid interfaces, Rev. Sci. Instrum. **74**, 4916 (2003).

[27] R. J. Mannheimer and R. S. Schechter, Shear-dependent surface rheological measurements of foam stabilizers in nonaqueous liquids, J. Colloid Interface Sci. **32**, 212 (1970).

[28] J. M. Lopez, R. Miraghaie, and A. H. Hirsa, Non-Newtonian behavior of an insoluble monolayer: Effects of inertia, J. Colloid Interface Sci. **248**, 103 (2002).

[29] A. Raghunandan, A. H. Hirsa, P. T. Underhill, and J. M. Lopez, Predicting Steady Shear Rheology of Condensed-Phase Monomolecular Films at the Air-Water Interface, Phys. Rev. Lett. **121**, 164502 (2018).

[30] P. T. Underhill, A. H. Hirsa, and J. M. Lopez, Modelling steady shear flows of Newtonian liquids with non-Newtonian interfaces, J. Fluid Mech. **814**, 5 (2017).

[31] T. Bodnár, A. Sequeira, and M. Prosi, On the shear-thinning and viscoelastic effects of blood flow under various flow rates, Appl. Math. Comput. **217**, 5055 (2011).

[32] N. S. Akbar and S. Nadeem, Carreau fluid model for blood flow through a tapered artery with a stenosis, Ain Shams Eng. J. **5**, 1307 (2014).

[33] E. R. Morris, A. N. Cutler, S. B. Ross-Murphy, D. A. Rees, and J. Price, Concentration and shear rate dependence of viscosity in random coil polysaccharide solutions, Carbohydr. Polym. **1**, 5 (1981).

[34] F. L. Muller and J. F. Davidson, Rheology of shear thinning polymer solutions, Ind. Eng. Chem. Res. **33**, 2364 (1994).

[35] D. T. Wasan, L. Gupta, and M. K. Vora, Interfacial shear viscosity at fluid-fluid interface, AIChE J. **17**, 1287 (1971).

[36] A. Suzuki, A study on non-Newtonian surface viscosity, Kolloid Z. Z. Polym. **250**, 360 (1972).

[37] P. R. Amestoy, I. S. Duff, J. Y. L'Excellent, and J. Koster, A fully asynchronous multifrontal solver using distributed dynamic scheduling, SIAM J. Matrix Anal. Appl. **23**, 15 (2001).

[38] S. Fitzgibbon, E. Shaqfeh, G. G. Fuller, and T. Walker, Scaling analysis and mathematical theory of the interfacial stress rheometer, J. Rheol. **58**, 999 (2014).